The Astronomical Journal, 164:225 (12pp), 2022 November https://doi.org/10.3847/1538-3881/ac9472

A Transmission Spectrum of the Sub-Earth Planet L98-59 b in 1.1–1.7 μm

Mario Damiano[1], Renyu Hu[1,2], Thomas Barclay[3,4], Sebastian Zieba[5,6], Laura Kreidberg[5], Jonathan Brande[7], Knicole D. Colon[4,8], Giovanni Covone[9,10,11], Ian Crossfield[7], Shawn D. Domagal-Goldman[4], Thomas J. Fauchez[4,8,12], Stefano Fiscale[13], Francesco Gallo[9], Emily Gilbert[3,4,8,14,15], Christina L. Hedges[16,17], Edwin S. Kite[18], Ravi K. Kopparapu[4], Veselin B. Kostov[4,8,19], Caroline Morley[20], Susan E. Mullally[21], Daria Pidhorodetska[22], Joshua E. Schlieder[4], and Elisa V. Quintana[4]

[1] Jet Propulsion Laboratory, California Institute of Technology, Pasadena, CA 91109, USA; mario.damiano@jpl.nasa.gov
[2] Division of Geological and Planetary Sciences, California Institute of Technology, Pasadena, CA 91125, USA
[3] University of Maryland, Baltimore County, 1000 Hilltop Cir, Baltimore, MD 21250, USA
[4] NASA Goddard Space Flight Center, 8800 Greenbelt Rd, Greenbelt, MD 20771, USA
[5] Max-Planck-Institut für Astronomie (MPIA), Königstuhl 17, D-69117 Heidelberg, Germany
[6] Leiden Observatory, Leiden University, Niels Bohrweg 2, 2333CA Leiden, The Netherlands
[7] Department of Physics and Astronomy, University of Kansas, 1082 Malott, 1251 Wescoe Hall Dr, Lawrence, KS 66045, USA
[8] NASA GSFC Sellers Exoplanet Environments Collaboration, 8800 Greenbelt Rd, Greenbelt, MD 20771, USA
[9] Dipartimento di Fisica "E. Pancini," Università di Napoli Federico II, Via Cinthia I-80126 Naples, Italy
[10] INAF, Osservatorio Astronomico di Capodimonte, Salita Moiariello, Napoli, Italy
[11] INFN, Sezione di Napoli, C.U. Monte S. Angelo, Via Cinthia, I-80126 Napoli, Italy
[12] Goddard Earth Sciences Technology and Research (GESTAR), Universities Space Research Association (USRA), Columbia, MD 7178, USA
[13] Dipartimento di Scienze e Tecnologia, Università degli Studi di Napoli Parthenope, Naples, Italy
[14] Department of Astronomy and Astrophysics, University of Chicago, 5640 S. Ellis Ave, Chicago, IL 60637, USA
[15] The Adler Planetarium, 1300 South Lakeshore Dr, Chicago, IL 60605, USA
[16] Bay Area Environmental Research Institute, P.O. Box 25, Moffett Field, CA 94035, USA
[17] NASA Ames Research Center, Moffett Field, CA 94035, USA
[18] Department of the Geophysical Sciences, University of Chicago, Chicago, IL, USA
[19] SETI Institute, 189 Bernardo Ave, Suite 200, Mountain View, CA 94043, USA
[20] Department of Astronomy, University of Texas at Austin, Austin, TX, USA
[21] Space Telescope Science Institute, 3700 San Martin Dr, Baltimore, MD 21218, USA
[22] Department of Earth and Planetary Sciences, University of California, Riverside, CA, USA
Received 2022 March 16; revised 2022 September 1; accepted 2022 September 19; published 2022 October 31

Abstract

With the increasing number of planets discovered by the Transit Exoplanet Survey Satellite, the atmospheric characterization of small exoplanets is accelerating. L98-59 is an M-dwarf hosting a multiplanet system, and so far, four small planets have been confirmed. The innermost planet b is ∼15% smaller and ∼60% lighter than Earth, and should thus have a predominantly rocky composition. The Hubble Space Telescope observed five primary transits of L98-59 b in 1.1–1.7 μm, and here we report the data analysis and the resulting transmission spectrum of the planet. We measure the transit depths for each of the five transits and, by combination, we obtain a transmission spectrum with an overall precision of ∼20 ppm in for each of the 18 spectrophotometric channels. With this level of precision, the transmission spectrum does not show significant modulation, and is thus consistent with a planet without any atmosphere or a planet having an atmosphere and high-altitude clouds or haze. The scenarios involving an aerosol-free, H_2-dominated atmosphere with H_2O or CH_4 are inconsistent with the data. The transmission spectrum also disfavors, but does not rule out, an H_2O-dominated atmosphere without clouds. A spectral retrieval process suggests that an H_2-dominated atmosphere with HCN and clouds or haze may be the preferred solution, but this indication is nonconclusive. Future James Webb Space Telescope observations may find out the nature of the planet among the remaining viable scenarios.

Unified Astronomy Thesaurus concepts: Extrasolar rocky planets (511); Exoplanet atmospheres (487); Exoplanet atmospheric composition (2021); Transmission spectroscopy (2133); Astronomy data analysis (1858)

1. Introduction

Observational studies of the atmospheres on small and predominantly rocky exoplanets are picking up speed. The Hubble Space Telescope (HST) has measured the transmission spectra of several approximately Earth-sized exoplanets (e.g., De Wit et al. 2018; Zhang et al. 2018; Mugnai et al. 2021; Swain et al. 2021), and these measurements provide important context for planning observations with other telescopes such as JWST. On larger and volatile-rich exoplanets, HST was able to detect multiple chemical compounds such as H_2O, CH_4, TiO, and VO (e.g., Knutson et al. 2007, 2014; Swain et al. 2008, 2009; Fraine et al. 2014; Kreidberg et al. 2014; Evans et al. 2016; Sing et al. 2016; Tsiaras et al. 2016a, 2018, 2019; Damiano et al. 2017; Benneke et al. 2019). Together with the continuing planet discoveries by the Transit Exoplanet Survey Satellite (TESS; Ricker et al. 2015), we expect transit observations with HST and JWST to push the frontier of exoplanet atmospheric characterization to Earth-sized and likely rocky planets.

L98-59 is an M3V star hosting a planetary system of four planets (Cloutier et al. 2019; Demangeon et al. 2021). Hints of a possible fifth planet have been observed but it has not yet

Table 1
Parameters of L98-59 and the Planet b

Stellar Parameters (L98-59)		
$T_{\rm eff}$ [K]	3412 ± 49	Cloutier et al. (2019)
M_* [$M_\odot$]	0.312 ± 0.031	Cloutier et al. (2019)
R_* [$R_\odot$]	0.314 ± 0.014	Cloutier et al. (2019)
[Fe/H] [dex]	-0.5 ± 0.5	Cloutier et al. (2019)
$\log(g_*)$ [cgs]	4.94 ± 0.06	Cloutier et al. (2019)
Planetary parameters (L98-59 b)		
$T_{\rm eq}$ [K]	627 ± 35	
$M_{\rm p}$ [$M_\oplus$]	0.40 ± 0.16	Demangeon et al. (2021)
$R_{\rm p}$ [$R_\oplus$]	0.85 ± 0.054	Demangeon et al. (2021)
a [au]	0.02191 ± 0.00082	Demangeon et al. (2021)
Transit parameters (L98-59 b)		
T_0 [JD]	$2458366.17067 \pm 0.00035$	Demangeon et al. (2021)
Period [days]	2.2531136 ± 0.0000014	Demangeon et al. (2021)
$R_{\rm p}/R_*$	0.02512 ± 0.00068	Demangeon et al. (2021)
i [deg]	87.7 ± 0.8	Demangeon et al. (2021)

Note. The equilibrium temperature, $T_{\rm eq}$, is calculated by assuming zero albedo and efficient heat redistribution. The parameters used to calculate $T_{\rm eq}$ have been adopted from Demangeon et al. (2021).

been confirmed. The innermost planet, L98-59 b, is a rocky planet 15% smaller in size than the Earth. The planet completes its orbit around its star in ∼2.25 days and its equilibrium temperature is ∼627 K as it receives more irradiation compared to Earth (see Table 1 for the system parameters adopted in this work). High-precision radial-velocity measurements have determined that the planet has a mass of ∼40% Earth's, and the planet's mass and radius is consistent with interior-structure scenarios that range from a rocky body with no atmosphere to a planet with small but substantial gas layers (Demangeon et al. 2021). We are thus motivated to find out whether the planet has an atmosphere through spectroscopic observations.

HST has observed five primary transits of L98-59 b in the near-IR with the Wide Field Camera 3 (WFC3). In this letter, we report the data analysis and the extraction of the 1D transmission spectrum, and explore the possible atmospheric scenarios by interpreting the spectrum with a spectral retrieval algorithm. The letter is organized as follows: in Section 2, we describe two independent analyses that were used to reduce the data and extract the transmission spectrum. In Section 3, we report the extracted 1D spectra and the transit depths obtained from fitting the transit spectral and white-light curves. In Section 4, with a spectral analysis, we discuss the range of the atmospheric scenarios allowed by the spectrum and how future observations may further characterize the planet. We conclude in Section 5.

2. Methods

2.1. Observations

Five primary transits of L98-59 b have been observed by HST from 2020 February to 2021 February and the data are available from the MAST archive (Program ID: 15856; PI: T. Barclay[23]). HST recorded the spatially scanned spectroscopic images through the G141 grism. Each of the five visits contained four consecutive HST orbits and each exposure was recorded in a 522×522 pixels image with an exposure time of 69.617 s each. With this configuration, the maximum signal level was 2.6×10^4 electrons per pixel and the total scan length was approximately 300 pixels. The data set also contained, for calibration purposes, a nondispersed (direct) image of the target, obtained using the F130N filter.

2.2. Data Analysis

We have used two independent data reduction and analysis pipelines to analyze the data set.

Analysis A. We first used IRACLIS, which has been widely applied to analyze the transit observations of HST/WFC3 (e.g., Tsiaras et al. 2016a, 2016b, 2018; Damiano et al. 2017). The data reduction starts from the raw images and corrects for the bias, dark current, flat field, gain, sky background, and bad pixels. The images are then calibrated with a wavelength mapping and the signal is extracted from each image through a 2D fitting. As is commonly done with WFC3 data, the images of the first HST orbit of each visit are discarded to minimize detector systematics (e.g., Deming et al. 2013; Huitson et al. 2013; Haynes et al. 2015; Damiano et al. 2017). We have also discarded the first scan of each of the remaining orbits. The sequence of the signals extracted from the images composes the white and spectral (when a wavelength binning is taken into account) light curves.

We employed a parametric fitting for the white-light curve. In particular, the instrumental systematics (known as "ramps"; Kreidberg et al. 2014; Tsiaras et al. 2016a, 2016b; Damiano et al. 2017) that affect the WFC3 infrared detector and the light-curve model are fitted at the same time to the observed data to correct for systematics and calculate the transit depths. For the correction of the ramps we used an approach similar to Kreidberg et al. (2014), i.e., adopting an analytic function with two different types of ramps, short-term and long-term:

$$R(t) = (1 - r_a(t - t_v))(1 - r_{b1}e^{-r_{b2}(t-t_0)}) \quad (1)$$

where t is the midtime of each exposure, t_v is the time when the visit starts, t_0 is the time when each orbit starts, r_a is related to the long-term ramp, and r_{b1} and r_{b2} are related to the short-term ramp. This systematics function together with the light-curve model and the limb-darkening coefficients previously calculated are used as the fitting model for the observed white-light curves:

$$M(t) = n_w R(t) F(t) \quad (2)$$

where t represents the time, $R(t)$ is the systematics function (Equation (1)), $F(t)$ is the transit model calculated by using `pylightcurve` (Tsiaras et al. 2016b), and n_w is a normalization factor. Moreover, we note that due to the HST spatial scanning techniques (i.e., the telescope slews slowly along the cross-dispersion direction instead of staring at the target), the images related to the downward scanning direction have a different associated normalization factor compared to those recorded with an upward scanning (Tsiaras et al. 2016b). Therefore, the normalization factors are $n_{w,\rm for}$ and $n_{w,\rm rev}$ for forward and reverse scanning respectively.

To account for the limb-darkening effect, we adopted the Claret's formulation (Claret 2000; four-parametric expression). The coefficients have been calculated by using EXOTETHYS (Morello et al. 2020) and provided in Appendix A.

[23] Data set:10.17909/cphn-nc88.

We used Markov chain Monte Carlo (MCMC) statistical tool (the `python` package `emcee`; Foreman-Mackey et al. 2013) to fit the five white-light curves. 200 walkers have been deployed and 500,000 iterations have been considered (the first 200,000 iterations are considered to be burned to allow the chains to stabilize). The free parameters of the fitting are: the two normalization factors $n_{w,\mathrm{for}}$ and $n_{w,\mathrm{rev}}$; the three parameters describing the instrumental systematics in Equation (1), r_a, r_{b1}, and r_{b2}; the planetary and stellar radius ratio, $R_p/R_\star$; and, finally, the midtransit time, T_0.

Lastly, to fit the spectral light curves, for each wavelength bin we divided the spectral light curve by the white-light curve (Kreidberg et al. 2014), and fitted a linear trend simultaneously with a relative transit model. Also in this case we used MCMC to fit the model to the data points. For the spectral light curve, we used 100 walkers and considered only 50,000 iteration (first 20,000 were considered burned iterations) as the complexity of the fitting is lower than the white-light curve. When the spectral light curves are divided by the white one, the effect of the instrumental systematics, described in Equation (1), is also divided out. As such, the reduction of the number of iterations does not impact the convergence of the parameters. For the spectral-light-curve fitting the free parameters are: the two normalization factors of relative to forward and reverse scanning, $n_{w,\mathrm{for}}$ and $n_{w,\mathrm{rev}}$; the planetary and stellar radius ratio, $R_p/R_\star$; and, finally, the midtransit time, T_0.

Analysis B. We also used a custom pipeline described in Kreidberg et al. (2014, 2018) to reduce the `ima` data products which we accessed from the MAST archive. The `ima` (intermediate MultiAccum) files already had all calibrations applied (dark subtraction, linearity correction, and flat fielding) to each readout of the IR exposure. Every orbit of the observations started with an direct image, which we used to determine centroid position of the star on the detector.

We separately extracted each up-the-ramp sample and subtracted the background flux from them. The background flux was determined by taking the median flux of the pixels where the spectrum did not fall on. We used the optimal extraction routine presented in Horne (1986) to extract the spectra and then coadded the individual samples to get the final spectrum for each exposure. To correct for spectral drift, we cross-correlated the first exposure in every orbit with a reference spectrum consisting of the product of the bandpass of the WFC3/G141 instrument and a `PHOENIX`[24] stellar model (Allard et al. 2003) for L98-59 b. We used the PHOENIX stellar model which was the closest to the stellar parameters from (Cloutier et al. 2019), i.e., the one corresponding to $T_{\mathrm{eff}} = 3400$ K, $\log(g) = 5.00$ and MH $= -0.5$. Due to strong ramp-like features in the raw data caused by charge traps filling up in the detector (Zhou et al. 2017), we also removed the first orbit in every visit and the first exposure in every orbit, as in previous WFC3 analysis (Kreidberg et al. 2014).

Our fitting model $F_B(t)$ consists of a transit model $F_{\mathrm{transit}}(t)$ which is implemented in the open-source python package `batman` (Kreidberg 2015) and a systematic model $F_{\mathrm{sys}}(t)$ to fit for the WFC3 systematics:

$$F_B(t) = F_{\mathrm{transit}}(t)\, F_{\mathrm{sys}}(t). \tag{3}$$

The systematic model $F_{\mathrm{sys}}(t)$ consists of a visit long linear trend $F_{\mathrm{sys,visit}}(t)$ and an exponential ramp for each orbit $F_{\mathrm{sys,orbit}}(t)$:

$$\begin{aligned} F_{\mathrm{sys}}(t) &= F_{\mathrm{sys,visit}}(t)\, F_{\mathrm{sys,orbit}}(t) \\ &= (c\, S(t) + k\, t_{\mathrm{v}})\, (1 - \exp(-r_1\, t_{\mathrm{orb}} - r_2 - r_3\, t_{\mathrm{orb}}\, Q(t))), \end{aligned} \tag{4}$$

where t_v is the time since the first exposure in a visit and t_{orb} is the time since the first exposure in an orbit. The linear trend $F_{\mathrm{sys,visit}}(t)$ includes the flux constant c and the slope k. $S(t)$ accounts for the upstream–downstream effect (McCullough & MacKenty 2012), which leads to an alternating total flux between exposures with spatial scanning in the forward direction and exposures with reverse scans. We define this scale factor to be $S(t) = 1$ for forward scans and $S(t) = s$ for reverse scans. The exponential ramp parameters are r_1, r_2 and r_3. Because the first remaining orbit (hereafter "first orbit") in every visit exhibited a stronger exponential ramp than the following ones, we included a rectangular function $Q(t)$, where $Q(t) = 1$ for the first orbit in a visit, and $Q(t) = 0$ for the others. For the fits we allowed all systematic parameters (c, k, s, r_1, r_2, and r_3) to have different values from visit to visit. For the spectroscopic-light-curve fits, we additionally allowed these parameters to vary for every spectroscopic bin.

For the white-light-curve fit and the spectroscopic fits we fixed the orbital period P, ratio of semimajor axis to stellar radius a/R_s and the orbital inclination i to literature values (Demangeon et al. 2021). We also fixed the eccentricity to zero. For the white-light-curve fit we therefore fitted for the ratio of planet to stellar radius R_p/R_s, the transit time T_0 for each visit, a linear limb-darkening parameter u_1, and for the six different systematic parameters (c, k, s, r_1, r_2 and r_3) for each visit. For the spectroscopic-light-curve fits, we fixed the transit time T_0 of each visit to the best-fit values from the white-light-curve fit.

We used the MCMC Ensemble sampler package `emcee` (Foreman-Mackey et al. 2013) to estimate the parameters and their uncertainties for our model. We rescaled the uncertainties for every data point by a constant factor so that the reduced chi-squared is unity, to ensure we are not underestimating the uncertainties of our parameters. For the white-light curve and each spectroscopic light curve, we ran 12,000 steps and 80 walkers and disregarded the first half of the samples as burn-in. Finally, in Analysis B, we decided not to fit each visit's white-light curve independently; instead, we fitted them within the same instance by fitting for one R_p/R_s and five midtransit time T_0. Similarly, the spectral light curves for each wavelength bin from all visits have been fitted together.

3. Results

Figure 1 presents white-light curves corrected for instrument systematics and fitted by the transit model, based on Analysis A. The midtransit time and R_p/R_s are reported in Table 2. The residuals do not show correlated signals. We observed an increased scatter in the light curve of Visit 4, which resulted in greater uncertainty in R_p/R_s.

The derived 1D spectra from Analysis A are reported in Table 3, and the quality of the spectral-light-curve fits is reported in Appendix B. We observe that the standard deviation of the residuals is close to the photon noise limit, supporting

[24] https://archive.stsci.edu/hlsps/reference-atlases/cdbs/grid/phoenix/

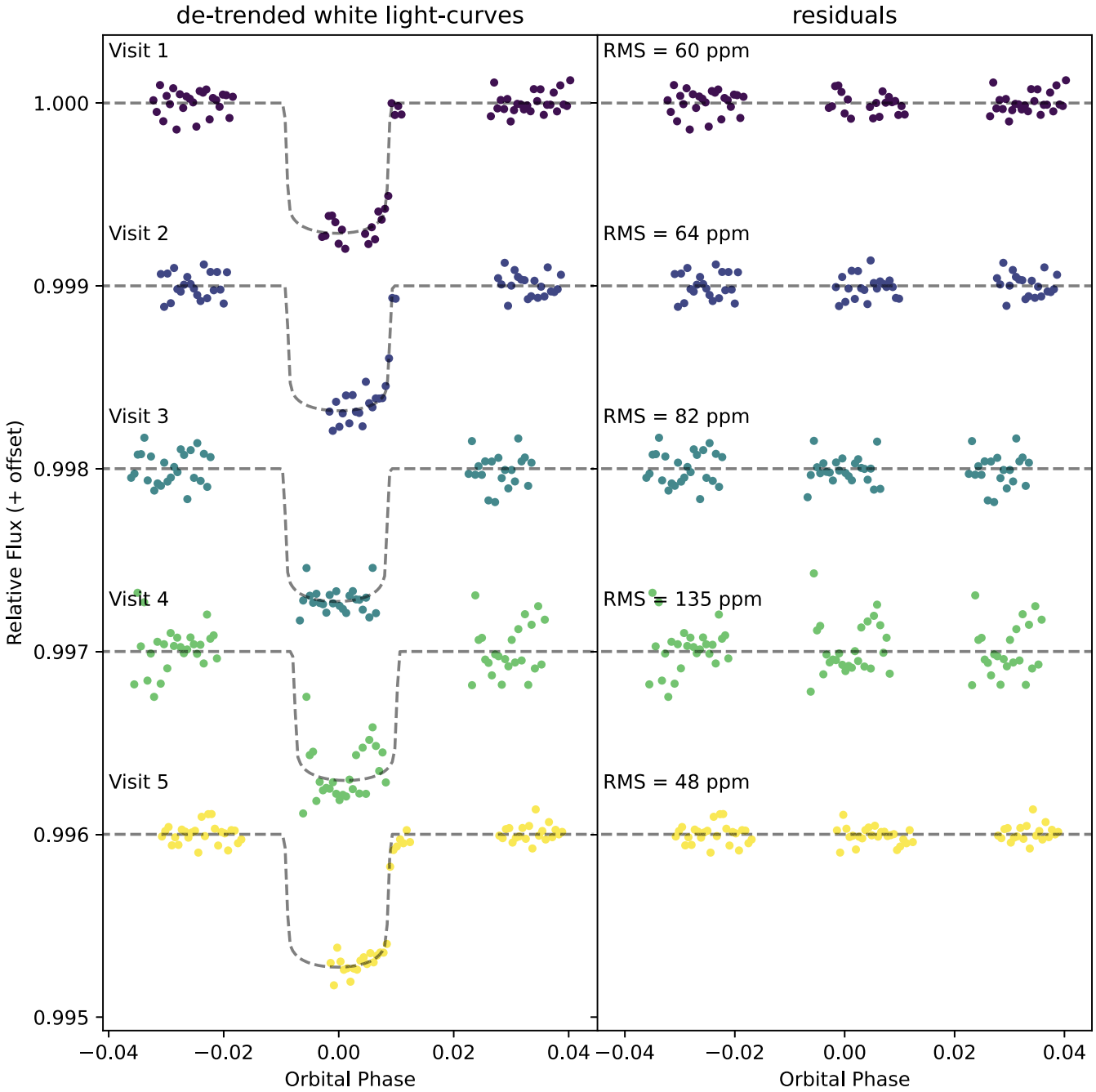

Figure 1. White-light curves of HST observations of L98-59 b transits. For each visit, the left panel shows the light curves from 2D images after correcting for systematics, and the right panel shows the residuals of the fit of the white-light curves. The dashed line depicts the best-fit transit model. A vertical shift of 0.001 is applied between the visits to better visualize the curves.

the practice to divide the spectral light curves by the white ones to remove instrumental systematics.

From Analysis B, we obtained a white-light-curve simultaneous fit to the five visits with an rms of 48 ppm. The midtransit time and R_p/R_s are also reported in Table 2, and they are comparable to the result from Analysis A. The derived 1D spectrum is reported in Table 4.

The resulting spectra from the two analyses are shown in Figure 2. For Analysis A, the weighted average of the single-visit spectra is calculated. The two methods provided consistent results within 1σ across the wavelength range, and the uncertainties provided by the two methods are also consistent.

4. Discussion

4.1. Plausible Planetary Scenarios

The transmission spectra do not show apparent modulation. The data are consistent with a flat spectrum where the transit depth does not change with wavelength with $\chi^2 = 17.8$ for a degree of freedom of 17. This means that the transmission spectra are consistent with a planet without any atmosphere (i.e., a bare-rock planet), or a planet with an atmosphere and high-altitude clouds or haze. For comparison, we have calculated the spectra of cloud-free H_2-dominated atmospheres with solar-abundance H_2O or CH_4, and they are clearly ruled

Table 2
Midtransit Time and R_p/R_s Fitted from White-light Curves for Both Analyses

Midpoint [BJD+2450000]	Analysis A	Analysis B
Visit 1	8888.89348 ± 0.00016	8888.8921 ± 0.0012
Visit 2	8947.47386 ± 0.00029	8947.4730 ± 0.0012
Visit 3	9120.9646 ± 0.0023	9120.9626 ± 0.0018
Visit 4	9179.542 ± 0.004	9179.5435 ± 0.0021
Visit 5	9269.66962 ± 0.00010	9269.6680 ± 0.0012
$(R_p/R_s)^2$ [ppm]		
Visit 1	663 ± 21	···
Visit 2	635 ± 26	···
Visit 3	676 ± 27	···
Visit 4	656 ± 36	···
Visit 5	676 ± 16	···
Combined	665.2 ± 11.7	642.6 ± 10.8

Note. For Analysis B a single value of R_p/R_s has been fitted simultaneously for all visits, while for Analysis A, the combined value of R_p/R_s refers to the weighted average of the single-visit values.

out by the observed spectra (Figure 3). We used TAU-REX (Al-Refaie et al. 2021) and the opacities included in EXO-TRANSMIT [25] (Freedman et al. 2008, 2014; Lupu et al. 2014; Kempton et al. 2017) to synthesize the model transmission spectra.

We have also tested whether the transmission spectrum of L98-59b would be consistent with a high mean molecular weight atmosphere. We found the spectra to be consistent with a cloud-free CO_2-dominated atmosphere with $\chi^2 = 21.0$ (Figure 3). Interestingly, the transmission spectrum does not favor an H_2O-dominated atmosphere. We found that an H_2O-dominated atmosphere without clouds or haze would be excluded with a p value of 0.1 ($\chi^2 = 23.6$). The reason for this potential inconsistency is that an H_2O-dominated atmosphere should cause a rise in the transit depth at ∼1.4 μm, which is absent from the data. This finding is somewhat surprising because an H_2O-dominated atmosphere was one of the most likely scenarios for this planet prior to the observations (Demangeon et al. 2021). On the other hand, the observed spectra can be consistent with an H_2O-dominated atmosphere if clouds are included ($\chi^2 = 18.1$), similar to the case of GJ 1214 b (Kreidberg et al. 2014).

To explore the potential atmospheric scenarios of the planet in a more systematic way, we used TAU-REX (Al-Refaie et al. 2021) to run a statistical inverse process to reveal the range of atmospheric conditions that would be consistent with the observed transmission spectrum. We adopted the results from Analysis A in the spectral retrieval. We assumed that the background atmosphere was dominated by molecular hydrogen and helium, but also allowed any gas of interest to take a mixing ratio of (almost) unity, effectively allowing, for example, an H_2O-, CO_2- or N_2-dominated atmosphere. We considered a broad range of molecules as candidate trace gases, including H_2O, CH_4, CO_2, CO, and HCN. Given the relatively narrow spectral range probed, we assumed an isothermal temperature profile and molecular abundances constant with pressure. We set log- or linear-uniform priors to the fitted parameters. These are the log mixing ratios of the molecules ($\log(10^{-12}) - \log(10^{-0.1})$), the temperature (100–800 K), the radius of the planet (0.038–0.15 $R_{\rm Jup}$), and the cloud top pressure (10^{-3}–10^{7} Pa). The retrieval model additionally has the opacity contribution from Rayleigh scattering and collision-induced absorption from H_2–H_2 and H_2–He pairs. We used MULTINEST (Feroz & Hobson 2008; Feroz et al. 2009, 2019; Buchner et al. 2014) as optimizer of the retrieval, which is the implementation of the *nested sampling* algorithm (Skilling 2004, 2006; Sivia & Skilling 2006). We set the number of live points to 600 which is safely higher than four times the number of free parameters, which are nine in total. Finally, we set the evidence tolerance to the standard value 0.5.

The spectral retrieval suggested an interesting scenario that involves an H_2-dominated atmosphere, clouds at $\sim 10^3$ Pa, and substantial presence of HCN (see Appendix C for the posterior distributions). The volume mixing ratio (VMR) of HCN is not well constrained, but rather, the likelihood for higher values ($>10^{-2.5}$) is greater than lower values. The model spectrum referring the median of posterior distributions that includes an H_2-dominated atmosphere with HCN and clouds is shown in Figure 3. For this scenario, we report a Bayesian log evidence of 165.27 ± 0.09. Meanwhile, the retrieval disfavors any presence of H_2O or CH_4, and does not yield any constraints on CO, CO_2, or N_2 (Appendix C). If HCN is not included as a candidate molecule in the retrieval, the retrieval converges to a flat spectrum with a Bayesian log evidence of 164.87 ± 0.09, slightly lower than the case with HCN. For completeness we have also run the retrieval for all the model discussed in this section, and the Bayesian log-evidence results are reported in Table 5. The relative values of the Bayesian evidence are consistent with the χ^2 metrics reported earlier.

4.2. Stellar Activity

While the initial discovery paper for the L98-59 planets indicated that no stellar variability was detected (Kostov et al. 2019), at least one flare is seen in subsequent TESS observations, and evidence of activity was identified in radial-velocity data observations (Cloutier et al. 2019; Demangeon et al. 2021). Stellar activity can potentially mimic or mask the detection of at atmospheric signal in transmission spectra (Pont et al. 2008; Bean et al. 2010; Sing et al. 2011; Aigrain et al. 2012; Huitson et al. 2013; Jordán et al. 2013; Kreidberg et al. 2014; McCullough et al. 2014; Barstow et al. 2015; Nikolov et al. 2015; Herrero et al. 2016; Zellem et al. 2017; Rackham et al. 2018, 2019; Barclay et al. 2021). This is a particular challenge for early–mid M-dwarf stars where the residuals from stellar H_2O absorption can cause issues in the interpretation of data from 1.1 to 1.7 μm. The rotation rate of L98-59 is slow, likely in the region of 80 days (Cloutier et al. 2019; Demangeon et al. 2021). Therefore, the star rotates minimally during the 0.9 hr transit of L98-59 b. This makes a potential contamination signal somewhat less likely. However, even slowly rotating spotted stars are not immune to contaminated transmission spectra owing to the transit light-source effect (Rackham et al. 2018).

All of the five observations of L98-59 b have consistent transmission spectra, which provides confidence that a single observation does not dominate the combined data and bias the conclusions (Appendix B). Furthermore, the characteristic bump of a contaminated spectrum at 1.4 μm due to H_2O in the stellar atmosphere (Barclay et al. 2021) is not observed for this planet. Therefore, while we cannot rule out that our observations contain some level of uncorrected stellar signal, we do not see any evidence for this.

[25] https://github.com/elizakempton/Exo_Transmit/tree/master/Opac

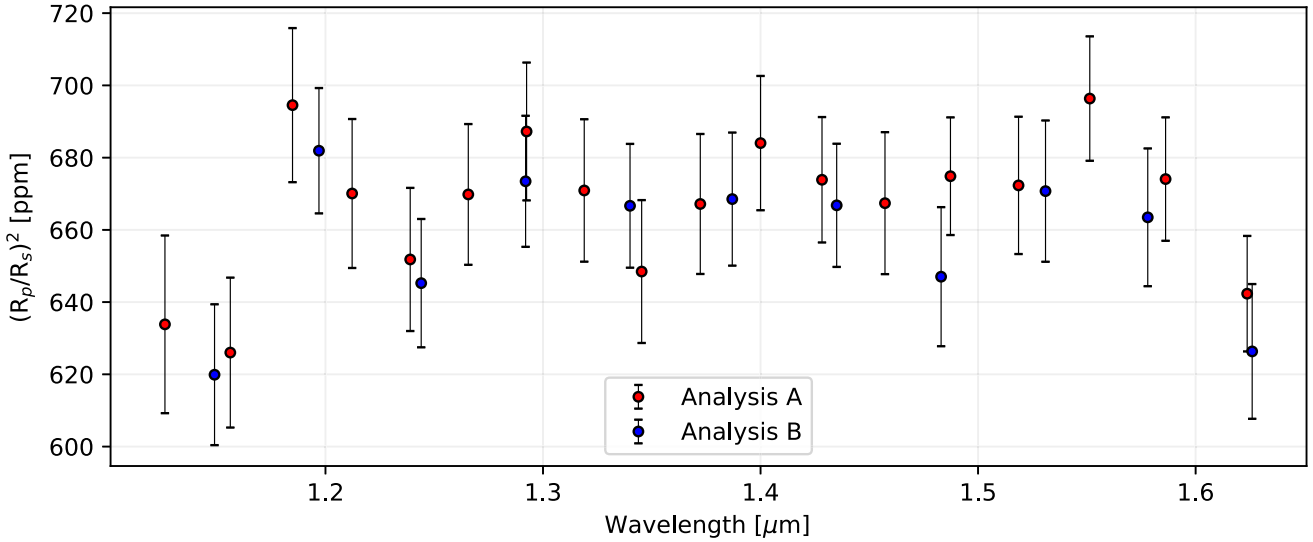

Figure 2. Transmission spectra of L98-59 b using the two independent methods described in Section 2. Each of the two spectra is the weighted average of the five single visits.

Table 3
Derived 1D Spectra ($(R_p/R_s)^2$) from the Five Visits of L98-59b using the Analysis A

Spectral Bins (nm)	V1	V2	V3	V4	V5	Weighted Average (ppm)
1110.8–1141.6	636 ± 65	600 ± 62	670 ± 57	617 ± 47	647 ± 51	634 ± 25
1141.6–1170.9	626 ± 63	664 ± 47	662 ± 39	596 ± 41	567 ± 52	626 ± 21
1170.9–1198.8	680 ± 46	724 ± 47	676 ± 48	657 ± 74	708 ± 39	695 ± 21
1198.8–1225.7	636 ± 38	642 ± 52	732 ± 75	711 ± 40	666 ± 45	670 ± 21
1225.7–1252.2	652 ± 57	600 ± 42	631 ± 38	686 ± 43	708 ± 47	652 ± 20
1252.2–1279.1	670 ± 44	586 ± 42	644 ± 44	745 ± 36	673 ± 62	670 ± 19
1279.1–1305.8	695 ± 41	649 ± 63	626 ± 46	700 ± 37	722 ± 37	687 ± 19
1305.8–1332.1	679 ± 40	569 ± 46	675 ± 43	677 ± 47	749 ± 45	671 ± 20
1332.1–1358.6	688 ± 53	635 ± 39	671 ± 49	580 ± 43	690 ± 42	648 ± 20
1358.6–1386.0	667 ± 57	558 ± 39	717 ± 36	726 ± 49	686 ± 45	667 ± 19
1386.0–1414.0	696 ± 44	612 ± 56	710 ± 35	626 ± 48	711 ± 35	684 ± 19
1414.0–1442.5	666 ± 60	666 ± 41	691 ± 32	664 ± 37	670 ± 36	674 ± 17
1442.5–1471.9	672 ± 52	693 ± 49	661 ± 37	643 ± 37	691 ± 52	667 ± 20
1471.9–1502.7	659 ± 40	652 ± 37	717 ± 33	665 ± 31	670 ± 48	675 ± 16
1502.7–1534.5	677 ± 56	675 ± 44	722 ± 42	611 ± 35	707 ± 42	672 ± 19
1534.5–1568.2	683 ± 38	751 ± 48	687 ± 34	700 ± 32	675 ± 48	696 ± 17
1568.2–1604.2	658 ± 43	638 ± 38	680 ± 33	727 ± 39	663 ± 39	674 ± 17
1604.2–1643.2	665 ± 49	632 ± 30	647 ± 37	636 ± 29	654 ± 45	642 ± 16

4.3. Prospects of Future Studies

L98-59 b is currently the lowest-mass exoplanet measured through stellar radial velocities, and the uncertainties of the measured planetary mass and radius permit the planetary scenarios of a rocky body without any substantial gas or ice, a planet with ∼20% water by mass, or a planet with a small H_2/He gas layer (Demangeon et al. 2021). It is thus particularly interesting to find out whether the planet has an atmosphere. Basic theoretical models suggest that sub-Earths in 2 day orbits should not have an atmosphere (e.g., Zahnle & Catling 2017). However, these models do not include many effects that might allow small, highly irradiated planets to exhibit an atmosphere, for example the low escape efficiency for CO_2-dominated atmospheres (Tian 2009; Johnstone et al. 2021). It is also plausible that the planet has retained some volatile through the early evolution (e.g., Kite & Schaefer 2021) or has a secondary atmosphere from volcanic outgassing (e.g., Kite & Barnett 2020). However, nonthermal escape processes may be very effective in removing the secondary atmosphere (e.g., Dong et al. 2018), and moreover, volcanic outgassing may shut down quickly on sub-Earth-mass planets (Kite et al. 2009).

If the planet does not have an atmosphere, its rocky surface could be spectroscopically detectable via Si-O features in 7–13 μm (Hu et al. 2012). Similar to the case of LHS 3844 b (Kreidberg et al. 2019), thermal emission spectroscopy using JWST's MIRI instrument may detect the signatures of ultramafic, basaltic, and granitoid surfaces on this planet and reveal its geologic histories.

If the planet is a water world, it should have a steam atmosphere given the level of irradiation (e.g., Turbet et al. 2020). A cloudless H_2O atmosphere is not favored by the transmission spectra reported here, but is not ruled out. Theoretical calculations suggest that the escape efficiency for pure-H_2O atmospheres is high, similar to that for pure-H_2 atmospheres, disfavoring retention of a pure-H_2O atmosphere (Johnstone 2020). A CO_2-dominated

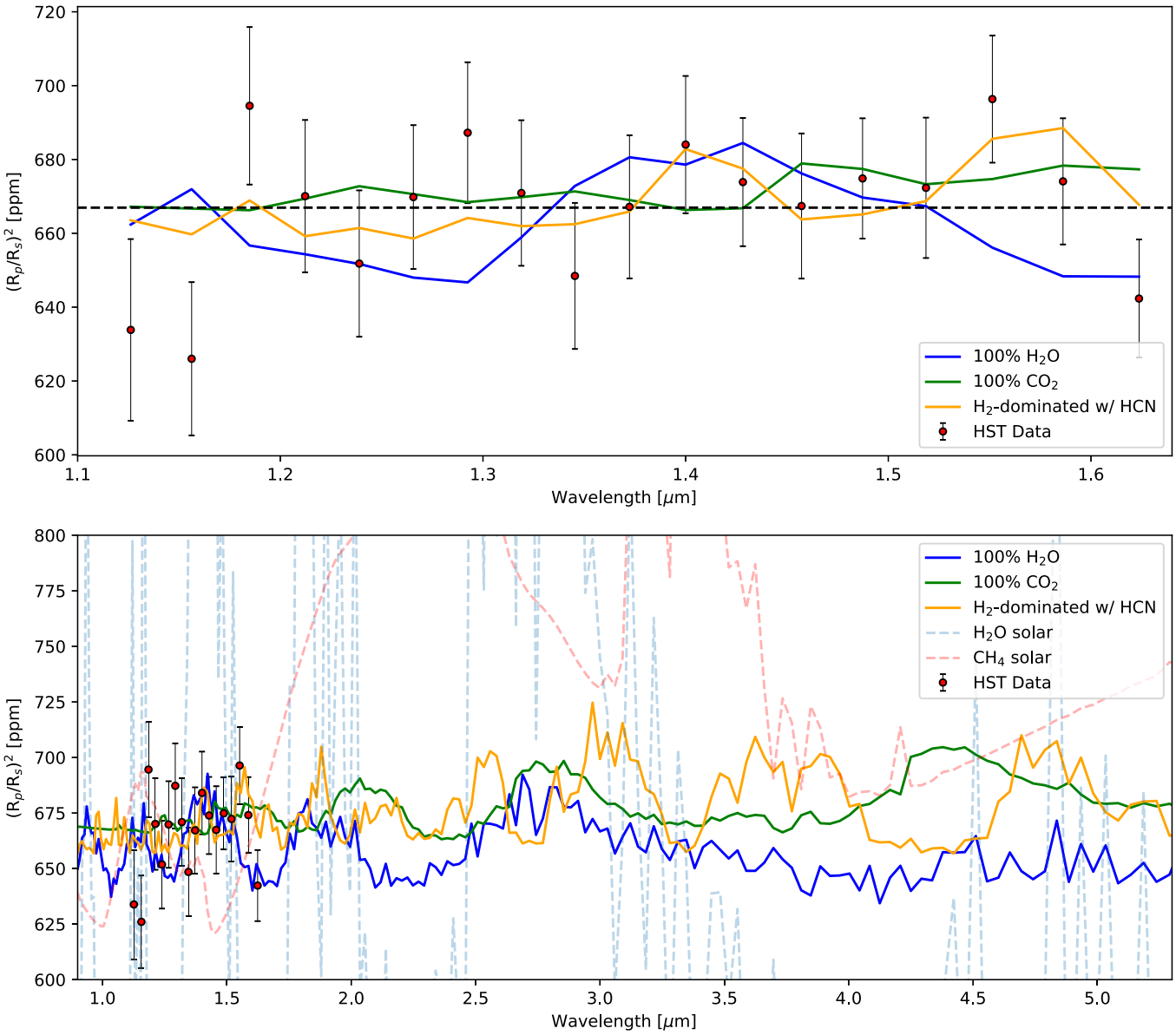

Figure 3. Top panel: transmission spectrum of L98-59 b in comparison with model scenarios. The scenarios of an H_2O- or CO_2-dominated atmosphere assume that the atmosphere does not have clouds or haze and has a temperature of the planet's equilibrium temperature. The H_2-dominated atmosphere model is the model calculated from the median of the posterior distribution shown in Figure 5. This model has HCN with a volume mixing ratio of 360 parts per million and clouds at 10^3 Pa in the atmosphere. Bottom panel: the HST data (Benneke et al. 2019; Tsiaras et al. 2019) comparing with atmospheric models of L98-59 b in the context of JWST observations. The dashed lines show the models with an H_2-dominated atmosphere and solar-abundance water and methane for comparison—these models are ruled out by the current data. The models permitted by the transmission spectrum reported here can be distinguished with JWST observations in ~1.5–5 μm.

atmosphere built up by volcanic outgassing would be consistent with the transmission spectra. Because of L98-59 b's low mass, this scenario would require that the planet start with much more CO_2 per unit mass than Earth or Venus according to the modeling of Kite & Barnett (2020). Therefore, if a CO_2-dominated atmosphere is detected in future, it would have major implications for the distribution and radial transport of Life-Essential Volatile Elements, including carbon, to distances close to the star (Dasgupta & Grewal 2019). The photometric precision achieved in this study is ~20 ppm per spectral channel, and a substantial improvement over this using HST may be very hard or inefficient. Figure 3 suggests that a precision of ~20 ppm in 1.5–5 μm at a moderate spectral resolution, which should be within the reach of the instruments on JWST (e.g., Beichman et al. 2014), could detect such a non-H_2-dominated atmosphere on the planet and characterize its bulk composition. Because of L98-59 b's small radius and known mass, such observations could provide a particularly powerful test for the models of planet-mass-dependent atmospheric retention and evolution on small planets.

Lastly, let us consider an H_2-dominated atmosphere having HCN and clouds. This scenario is favored by the retrieval of the transmission spectra as the statistical convergence tries to find the best model that fits the bump at 1.55 μm. The retrieval selects HCN in an H_2-dominated atmosphere and then it also invokes a cloud deck to produce an otherwise flat spectrum. This H_2-dominated atmosphere cannot be massive because, for the equilibrium temperature of ~600 K, an H_2-dominated atmosphere would already have a thickness of 0.4 $R_\oplus$ from 0.001 to 1 bar. To keep the H_2-dominated atmosphere small but existing is a fine-tuning problem as there is no known feedback

Table 4
Derived 1D Spectrum ($(R_p/R_s)^2$) from the Five Visits of L98-59b using the Analysis B

Spectral bins (nm)	$(R_p/R_s)^2$ (ppm)
1125.0–1173.0	620 ± 20
1173.0–1220.5	682 ± 17
1220.5–1268.0	645 ± 18
1268.0–1316.0	673 ± 18
1316.0–1363.5	667 ± 17
1363.5–1411.0	669 ± 18
1411.0–1459.0	667 ± 17
1459.0–1507.0	647 ± 19
1507.0–1554.5	671 ± 20
1554.5–1602.0	663 ± 19
1602.0–1650.0	626 ± 19

Note. The spectral light curves of the five visits are fit together to produce the combined constraints on $(R_p/R_s)^2$ for each wavelength bin.

Table 5
Bayesian log evidence, log(EV), Resulting from the Retrieval Process to the 1D Spectrum when Different Atmospheric Scenarios are Considered

Scenario	log(EV)
H_2-dominated atmosphere + clouds + HCN	165.44 ± 0.09
H_2-dominated atmosphere + clouds + H_2O + CH_4 + HCN + CO_2 + CO + N_2	165.27 ± 0.09
Fully clouded—flat spectrum	164.87 ± 0.09
CO_2-dominated atmosphere cloud free	164.86 ± 0.09
H_2O-dominated atmosphere + clouds	164.86 ± 0.09
H_2O-dominated atmosphere cloud free	160.93 ± 0.09

mechanism that stabilizes the mass of the atmosphere. Is a small H_2-dominated atmosphere a plausible scenario from the atmospheric evolution point of view? It is possible that most of the initial endowment of hydrogen has been lost during early evolutions (e.g., Misener & Schlichting 2021), and most of the remaining hydrogen is partitioned into the magma ocean (Kite et al. 2020; Gaillard et al. 2022). Volcanoes can release H_2-dominated gases into the atmosphere from the mantle (Liggins et al. 2020), and outgassing from impactors may also release H_2-dominated gases (Schaefer & Fegley 2017). Therefore, it would be worthwhile to pursue the hint of HCN suggested in this scenario. HCN is a common photochemical product in temperate, H_2-dominated atmospheres (Hu 2021) as well as in hot, N_2-dominated atmospheres (Miguel 2019). Warm atmospheres on rocky exoplanets with volcanic outgassing could also have HCN (Swain et al. 2021). There have been debated reports of HCN from exoplanet transit observations (Tsiaras et al. 2016a; Swain et al. 2021), and here, the rise of the transit depth between 1.5 and 1.6 μm has been found by two data analyses and is most naturally explained as the HCN absorption (Figure 3). This HCN, along with other possible scenarios discussed above, could be confirmed or refuted by observing the planet at longer wavelengths.

The other two detected planets in the L98-59 system (planets c and d) have been observed by HST within the program 15856 and the findings will be reported in a separate paper (T. Barclay et al. 2022, in preparation). Moreover, JWST will observe the planets c and d in 0.6–5 μm through multiple programs in Cycle 1. The L98-59 system is poised to become one of best characterized exoplanetary systems with multiple small planets. Comparing the transmission spectra of the three planets could reveal system-wide trends in the atmospheric composition and thus volatile retention.

5. Conclusion

In the paper, we report the transmission spectra of the warm sub-Earth-sized exoplanet L98-59 b in 1.1–1.7 μm, obtained by multiple-visit observations of the HST. We applied two independent data analysis pipelines and obtained consistent results. Combining five visits, we achieved a photometric precision of ∼20 ppm per spectral channel, with 18 channels in 1.1–1.7 μm ($R \sim 50$), making the transmission spectrum reported here one of the most precise measurements from an exoplanet (e.g., Kreidberg et al. 2014; Benneke et al. 2019; Tsiaras et al. 2019). The spectrum does not show significant modulation, and thus rules out a cloud-free H_2-dominated atmosphere with solar abundance of H_2O or CH_4. The spectrum also does not favor a cloud-free H_2O-dominated atmosphere. In addition to the null hypothesis (i.e., a bare-rock planet or an atmosphere with high-altitude clouds or haze), the spectrum is consistent with a cloud-free CO_2-dominated atmosphere or a small H_2-dominated atmosphere with HCN and clouds/haze. JWST observations of the planet at the precision of ∼20 ppm per spectral channel in a wide wavelength range could test these atmospheric scenarios and thus determine the nature of the planet. As a sub-Earth-sized planet, L98-59 b provides a valuable opportunity to test the volatile retention and evolution on small and irradiated exoplanets.

We thank A. Youngblood for assistance with the HST observations. This research is based on observations made with the NASA/ESA Hubble Space Telescope obtained from the Space Telescope Science Institute, which is operated by the Association of Universities for Research in Astronomy, Inc., under NASA contract NAS 5-26555. These observations are associated with program 15856. Support for program #15856 was provided by NASA through a grant from the Space Telescope Science Institute. This work was supported by the GSFC Sellers Exoplanet Environments Collaboration (SEEC), which is funded by the NASA Planetary Science Divisions Internal Scientist Funding Mode. The material is based on work supported by NASA under award No. 80GSFC21M0002. Part of the research was carried out at the Jet Propulsion Laboratory, California Institute of Technology, under a contract with the National Aeronautics and Space Administration.

Appendix A
Limb-darkening Coefficients

We used the Claret (2000) formulation for the limb-darkening effect. We calculated the four coefficients per spectral bins by using the EXOTETHYS python package. The coefficients are reported in Table 6.

Table 6
Spectral Bins and Limb-darkening Coefficients used in the Analysis A

Spectral Bins (nm)	a1	a2	a3	a4
1110.8–1141.6	1.28798093	−1.05907762	0.51823029	−0.0874053
1141.6–1170.9	1.28615323	−1.08744839	0.54951993	−0.09832113
1170.9–1198.8	1.29932409	−1.153228	0.62233941	−0.12612099
1198.8–1225.7	1.31403541	−1.20359881	0.66336835	−0.13702432
1225.7–1252.2	1.3216165	−1.24503919	0.71220673	−0.15662467
1252.2–1279.1	1.31087844	−1.22725216	0.6846187	−0.14247216
1279.1–1305.8	1.33205793	−1.32351788	0.80287643	−0.19154707
1305.8–1332.1	1.33327291	−1.34653724	0.82282639	−0.19646486
1332.1–1358.6	1.35830426	−1.43403262	0.91975243	−0.23435426
1358.6–1386.0	1.35014645	−1.4334713	0.9180878	−0.23234897
1386.0–1414.0	1.34613423	−1.44645255	0.93259913	−0.23707517
1414.0–1442.5	1.34866834	−1.47233056	0.95865921	−0.24580419
1442.5–1471.9	1.38009113	−1.58464562	1.09298133	−0.30172869
1471.9–1502.7	1.34297544	−1.51871236	1.02049438	−0.27172675
1502.7–1534.5	1.31575231	−1.47873437	0.97919057	−0.25523316
1534.5–1568.2	1.32973852	−1.56395607	1.08417177	−0.29880839
1568.2–1604.2	1.29595229	−1.52289987	1.04537638	−0.28498663
1604.2–1643.2	1.28150047	−1.58351836	1.14303257	−0.32898329

Appendix B
Single-visit Transmission Spectra

Following the extraction and correction of the white-light curves (see Sections 2 and 3), we fitted the spectral light curves to derive the 1D transmission spectrum. Figure 4 shows the 1D transmission spectrum derived by using Analysis A for each of the five visits and and the combined weighted average. In Table 7, we report statistical diagnostics for each wavelength channel from the five visits. The standard deviation relative to the photon noise limit, $\overline{\sigma}$, is very close to unity.

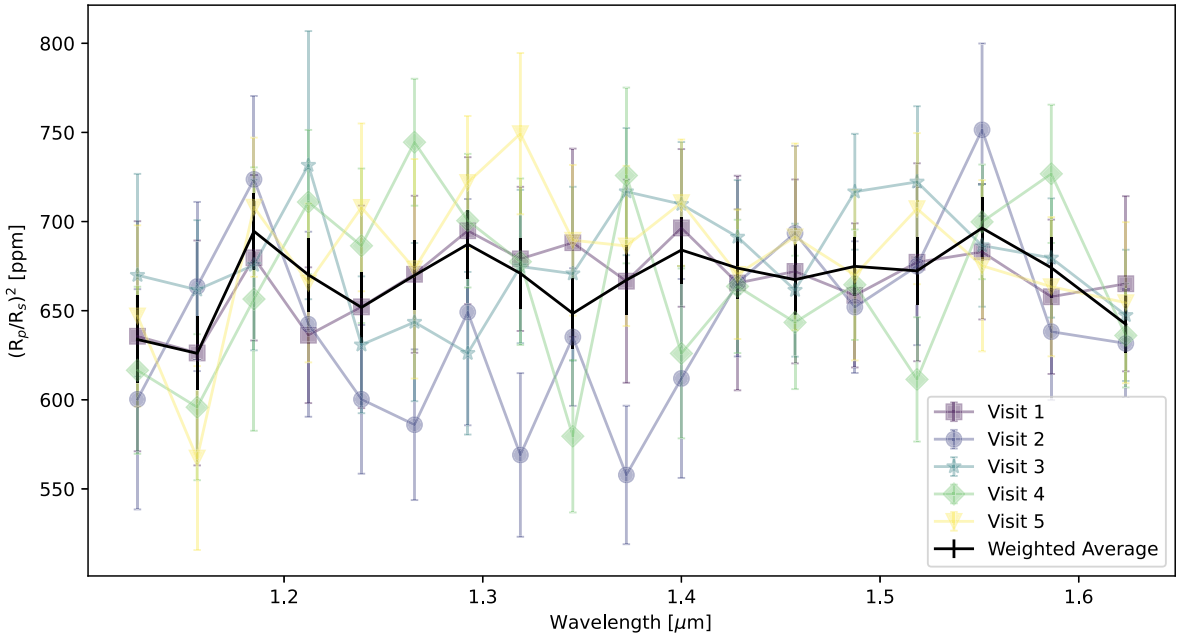

Figure 4. Colored: calculated 1D transmission spectrum of L98-59 b for each of the five HST visits resulting from the data analysis A described in Section 2. Black: weighted average combined transmission spectrum.

Table 7
Spectral Bins and Residuals Diagnostics for the each Wavelength Channel for the Spectral Light Curves Processed using Analysis A

Spectral Bins (nm)	Rms (ppm)	$\overline{\chi^2}$	$\overline{\sigma}$	R_2
1110.8–1141.6	170 ± 16	1.062 ± 0.004	1.17 ± 0.11	0.21 ± 0.08
1141.6–1170.9	155 ± 22	1.066 ± 0.008	1.09 ± 0.16	0.08 ± 0.04
1170.9–1198.8	152 ± 13	1.066 ± 0.005	1.10 ± 0.09	0.16 ± 0.08
1198.8–1225.7	170 ± 57	1.062 ± 0.004	1.25 ± 0.42	0.15 ± 0.05
1225.7–1252.2	137 ± 12	1.066 ± 0.005	1.02 ± 0.09	0.13 ± 0.06
1252.2–1279.1	147 ± 22	1.062 ± 0.004	1.11 ± 0.17	0.13 ± 0.07
1279.1–1305.8	135 ± 6	1.064 ± 0.008	1.04 ± 0.04	0.12 ± 0.05
1305.8–1332.1	136 ± 7	1.064 ± 0.005	1.05 ± 0.05	0.12 ± 0.08
1332.1–1358.6	145 ± 9	1.064 ± 0.005	1.11 ± 0.08	0.10 ± 0.02
1358.6–1386.0	152 ± 26	1.062 ± 0.004	1.17 ± 0.19	0.09 ± 0.05
1386.0–1414.0	144 ± 19	1.064 ± 0.005	1.10 ± 0.15	0.10 ± 0.06
1414.0–1442.5	137 ± 15	1.054 ± 0.012	1.05 ± 0.12	0.17 ± 0.08
1442.5–1471.9	140 ± 10	1.054 ± 0.015	1.09 ± 0.08	0.12 ± 0.07
1471.9–1502.7	126 ± 7	1.062 ± 0.004	1.00 ± 0.06	0.15 ± 0.06
1502.7–1534.5	135 ± 6	1.062 ± 0.004	1.08 ± 0.05	0.13 ± 0.05
1534.5–1568.2	137 ± 17	1.064 ± 0.005	1.11 ± 0.14	0.13 ± 0.07
1568.2–1604.2	122 ± 8	1.062 ± 0.004	1.01 ± 0.06	0.14 ± 0.08
1604.2–1643.2	132 ± 25	1.064 ± 0.005	1.11 ± 0.21	0.10 ± 0.06

Note. Rms: root mean squared of residuals; $\overline{\chi^2}$: reduced χ^2; $\overline{\sigma}$: standard deviation relative to the photon noise limit; and R_2: auto-correlation. The diagnostics are presented as the mean and the standard deviation of the five visits.

Appendix C
Posterior Distributions

The interpretation of the 1D spectrum shown in Figure 2 has led to multiple scenarios that cannot be excluded. However, if the planet retains a light atmosphere, i.e., an H_2-dominated atmosphere, the statistical interpretation of the spectrum suggests that a significant amount of HCN might be present. We show the median-fit model from the spectral retrieval in Figure 3 (orange line) and report the full posterior distributions here in Figure 5.

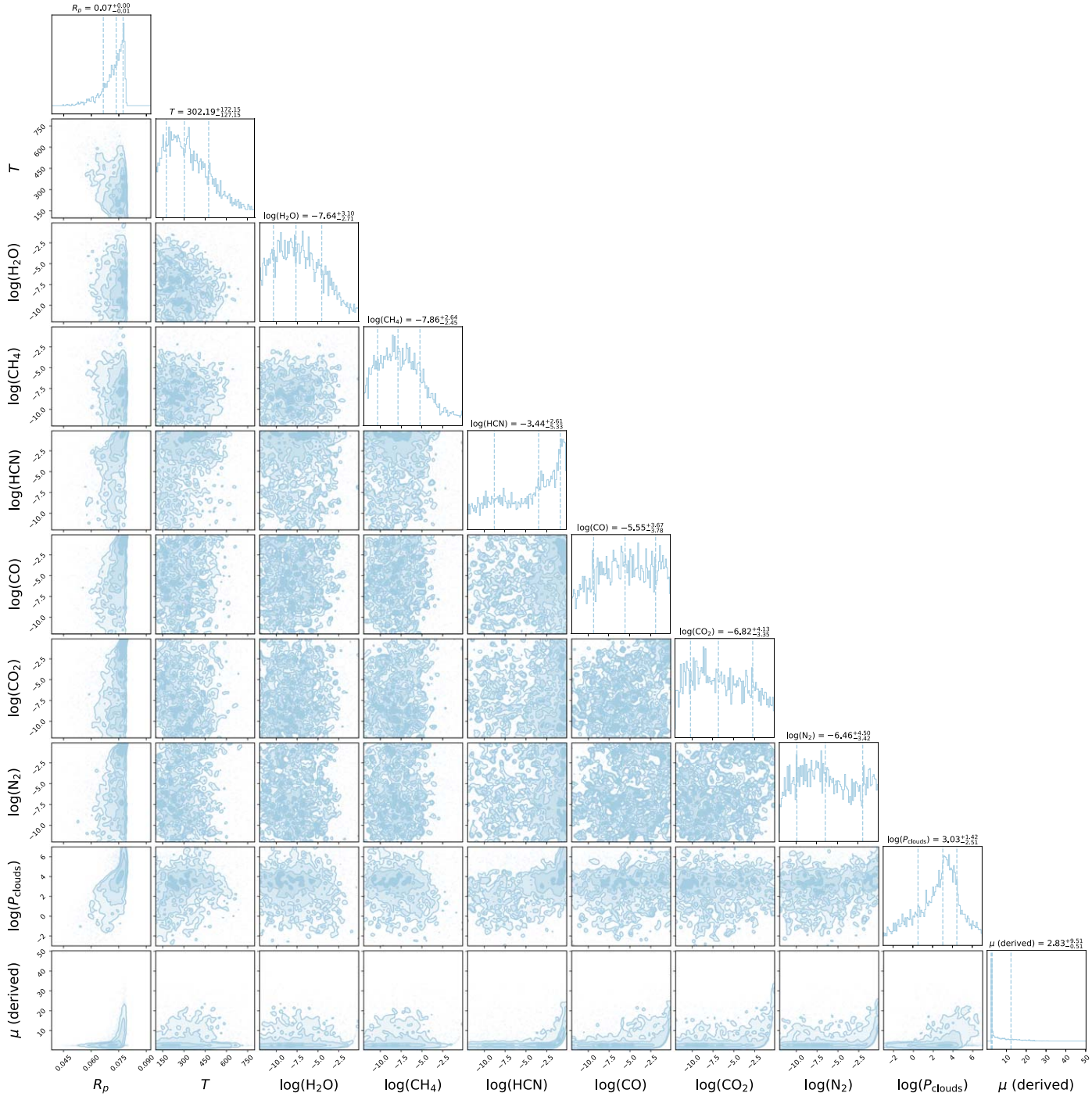

Figure 5. Posterior distributions of the retrieval on the 1D transmission spectrum of L98-59 b. The result suggests a light atmosphere (H_2-dominated) with clouds or haze and also hints the presence of HCN. The volume mixing ratio (VMR) of HCN has a distribution peak toward high values, but is otherwise not well constrained. All the other gases considered in the fitting show VMR distributions toward low values or completely flat, suggesting their absence in the atmosphere or a presence below the cloud deck not detectable by transmission spectroscopy. The parameter R_p in is defined as the radius at the bottom of the atmosphere, and therefore, when the atmosphere is more extended, the smaller this value must be to maintain consistency with the apparent radius of the planet.

ORCID iDs

Mario Damiano https://orcid.org/0000-0002-1830-8260
Renyu Hu https://orcid.org/0000-0003-2215-8485
Thomas Barclay https://orcid.org/0000-0001-7139-2724
Sebastian Zieba https://orcid.org/0000-0003-0562-6750
Laura Kreidberg https://orcid.org/0000-0003-0514-1147
Jonathan Brande https://orcid.org/0000-0002-2072-6541
Knicole D. Colon https://orcid.org/0000-0001-8020-7121
Giovanni Covone https://orcid.org/0000-0002-2553-096X
Shawn D. Domagal-Goldman https://orcid.org/0000-0003-0354-9325
Thomas J. Fauchez https://orcid.org/0000-0002-5967-9631
Stefano Fiscale https://orcid.org/0000-0001-8371-8525
Emily Gilbert https://orcid.org/0000-0002-0388-8004
Christina L. Hedges https://orcid.org/0000-0002-3385-8391
Edwin S. Kite https://orcid.org/0000-0002-1426-1186
Ravi K. Kopparapu https://orcid.org/0000-0002-5893-2471
Veselin B. Kostov https://orcid.org/0000-0001-9786-1031
Caroline Morley https://orcid.org/0000-0002-4404-0456
Susan E. Mullally https://orcid.org/0000-0001-7106-4683
Daria Pidhorodetska https://orcid.org/0000-0001-9771-7953
Joshua E. Schlieder https://orcid.org/0000-0001-5347-7062
Elisa V. Quintana https://orcid.org/0000-0003-1309-2904

References

Aigrain, S., Pont, F., & Zucker, S. 2012, MNRAS, 419, 3147
Allard, F., Guillot, T., Ludwig, H.-G., et al. 2003, in IAU Symp. 211, Brown Dwarfs, ed. E. Martín (San Francisco, CA: ASP), 325
Al-Refaie, A. F., Changeat, Q., Waldmann, I. P., & Tinetti, G. 2021, ApJ, 917, 37
Barclay, T., Kostov, V. B., Colón, K. D., et al. 2021, AJ, 162, 300
Barstow, J. K., Aigrain, S., Irwin, P. G. J., Kendrew, S., & Fletcher, L. N. 2015, MNRAS, 448, 2546
Bean, J. L., Miller-Ricci Kempton, E., & Homeier, D. 2010, Natur, 468, 669
Beichman, C., Benneke, B., Knutson, H., et al. 2014, PASP, 126, 1134
Benneke, B., Wong, I., Piaulet, C., et al. 2019, ApJL, 887, L14
Buchner, J., Georgakakis, A., Nandra, K., et al. 2014, A&A, 564, A125
Claret, A. 2000, A&A, 363, 1081
Cloutier, R., Astudillo-Defru, N., Bonfils, X., et al. 2019, A&A, 629, A111
Damiano, M., Morello, G., Tsiaras, A., Zingales, T., & Tinetti, G. 2017, AJ, 154, 39
Dasgupta, R., & Grewal, D. S. 2019, Deep Carbon: Past to Present (Cambridge: Cambridge Univ. Press), 4
De Wit, J., Wakeford, H. R., Lewis, N. K., et al. 2018, NatAs, 2, 214
Demangeon, O. D. S., Zapatero Osorio, M. R., Alibert, Y., et al. 2021, A&A, 653, A41
Deming, D., Wilkins, A., McCullough, P., et al. 2013, ApJ, 774, 95
Dong, C., Jin, M., Lingam, M., et al. 2018, PNAS, 115, 260
Evans, T. M., Sing, D. K., Wakeford, H. R., et al. 2016, ApJL, 822, L4
Feroz, F., & Hobson, M. P. 2008, MNRAS, 384, 449
Feroz, F., Hobson, M. P., & Bridges, M. T. B. 2009, MNRAS, 398, 1601
Feroz, F., Hobson, M. P., Cameron, E., & Pettitt, A. N. 2019, DOAJ, 2, 10
Foreman-Mackey, D., Hogg, D. W., Lang, D., & Goodman, J. 2013, PASP, 125, 306
Fraine, J., Deming, D., Benneke, B., et al. 2014, Natur, 513, 526
Freedman, R. S., Lustig-Yaeger, J., Fortney, J. J., et al. 2014, ApJS, 214, 25
Freedman, R. S., Marley, M. S., & Lodders, K. 2008, ApJS, 174, 504
Gaillard, F., Bernadou, F., Roskosz, M., et al. 2022, E&PSL, 577, 117255
Haynes, K., Mandell, A. M., Madhusudhan, N., Deming, D., & Knutson, H. 2015, ApJ, 806, 146
Herrero, E., Ribas, I., Jordi, C., et al. 2016, A&A, 586, A131
Horne, K. 1986, PASP, 98, 609
Hu, R. 2021, ApJ, 921, 27
Hu, R., Ehlmann, B. L., & Seager, S. 2012, ApJ, 752, 7
Huitson, C. M., Sing, D. K., Pont, F., et al. 2013, MNRAS, 434, 3252
Johnstone, C. P. 2020, ApJ, 890, 79
Johnstone, C. P., Lammer, H., Kislyakova, K. G., Scherf, M., & Güdel, M. 2021, E&PSL, 576, 117197
Jordán, A., Espinoza, N., Rabus, M., et al. 2013, ApJ, 778, 184
Kempton, E. M. R., Lupu, R., Owusu-Asare, A., Slough, P., & Cale, B. 2017, PASP, 129, 044402
Kite, E. S., & Barnett, M. N. 2020, PNAS, 117, 18264
Kite, E. S., Fegley, B., Jr., Schaefer, L., & Ford, E. B. 2020, ApJ, 891, 111
Kite, E. S., Manga, M., & Gaidos, E. 2009, ApJ, 700, 1732
Kite, E. S., & Schaefer, L. 2021, ApJL, 909, L22
Knutson, H. A., Benneke, B., Deming, D., & Homeier, D. 2014, Natur, 505, 66
Knutson, H. A., Charbonneau, D., Noyes, R. W., Brown, T. M., & Gilliland, R. L. 2007, ApJ, 655, 564
Kostov, V. B., Schlieder, J. E., Barclay, T., et al. 2019, AJ, 158, 32
Kreidberg, L. 2015, PASP, 127, 1161
Kreidberg, L., Bean, J. L., Désert, J.-M., et al. 2014, Natur, 505, 69
Kreidberg, L., Koll, D. D., Morley, C., et al. 2019, Natur, 573, 87
Kreidberg, L., Line, M. R., Parmentier, V., et al. 2018, AJ, 156, 17
Liggins, P., Shorttle, O., & Rimmer, P. B. 2020, E&PSL, 550, 116546
Lupu, R. E., Zahnle, K., Marley, M. S., et al. 2014, ApJ, 784, 27
McCullough, P., & MacKenty, J. 2012, Considerations for using Spatial Scans with WFC3, Space Telescope WFC Instrument Science Report
McCullough, P. R., Crouzet, N., Deming, D., & Madhusudhan, N. 2014, ApJ, 791, 55
Miguel, Y. 2019, MNRAS, 482, 2893
Misener, W., & Schlichting, H. E. 2021, MNRAS, 503, 5658
Morello, G., Claret, A., Martin-Lagarde, M., et al. 2020, AJ, 159, 75
Mugnai, L. V., Modirrousta-Galian, D., Edwards, B., et al. 2021, AJ, 161, 284
Nikolov, N., Sing, D. K., Burrows, A. S., et al. 2015, MNRAS, 447, 463
Pont, F., Knutson, H., Gilliland, R. L., Moutou, C., & Charbonneau, D. 2008, MNRAS, 385, 109
Rackham, B. V., Apai, D., & Giampapa, M. S. 2018, ApJ, 853, 122
Rackham, B. V., Apai, D., & Giampapa, M. S. 2019, AJ, 157, 96
Ricker, G. R., Winn, J. N., Vanderspek, R., et al. 2015, JATIS, 1, 014003
Schaefer, L., & Fegley, B. 2017, ApJ, 843, 120
Sing, D. K., Fortney, J. J., Nikolov, N., et al. 2016, Natur, 529, 59
Sing, D. K., Pont, F., Aigrain, S., et al. 2011, MNRAS, 416, 1443
Sivia, D., & Skilling, J. 2006, Data Analysis A Bayesian Tutorial (Oxford: Oxford Univ. Press)
Skilling, J. 2004, in AIP Conf. Ser. 735, Bayesian Inference and Maximum Entropy Methods in Science and Engineering: 24th International Workshop on Bayesian Inference and Maximum Entropy Methods in Science and Engineering, ed. R. Fischer, R. Preuss, & U. V. Toussaint (Melville, NY: AIP), 395
Skilling, J. 2006, BayAn, 1, 833
Swain, M. R., Estrela, R., Roudier, G. M., et al. 2021, AJ, 161, 213
Swain, M. R., Tinetti, G., Vasisht, G., et al. 2009, ApJ, 704, 1616
Swain, M. R., Vasisht, G., & Tinetti, G. 2008, Natur, 452, 329
Tian, F. 2009, ApJ, 703, 905
Tsiaras, A., Rocchetto, M., Waldmann, I. P., et al. 2016a, ApJ, 820, 99
Tsiaras, A., Waldmann, I. P., Rocchetto, M., et al. 2016b, ApJ, 832, 202
Tsiaras, A., Waldmann, I. P., Tinetti, G., Tennyson, J., & Yurchenko, S. N. 2019, NatAs, 3, 1086
Tsiaras, A., Waldmann, I. P., Zingales, T., et al. 2018, AJ, 155, 156
Turbet, M., Bolmont, E., Ehrenreich, D., et al. 2020, A&A, 638, A41
Zahnle, K. J., & Catling, D. C. 2017, ApJ, 843, 122
Zellem, R. T., Swain, M. R., Roudier, G., et al. 2017, ApJ, 844, 27
Zhang, Z., Zhou, Y., Rackham, B. V., & Apai, D. 2018, AJ, 156, 178
Zhou, Y., Apai, D., Lew, B. W. P., & Schneider, G. 2017, AJ, 153, 243